



Universiteit
Leiden
The Netherlands

Near-infrared phototransistor based on graphene/C60/PbPc heterojunction with tunable bidirectional photoresponse

Dai, Q.; Hu, G.; Wenli, L.V.; Xu, S.; Lei, S.; Schneider, G.F.; ... ; Peng, Y.

Citation

Dai, Q., Hu, G., Wenli, L. V., Xu, S., Lei, S., Schneider, G. F., ... Peng, Y. (2022). Near-infrared phototransistor based on graphene/C60/PbPc heterojunction with tunable bidirectional photoresponse. *Advanced Materials Interfaces*. doi:10.1002/admi.202200116

Version: Publisher's Version

License: [Licensed under Article 25fa Copyright Act/Law \(Amendment Taverne\)](#)

Downloaded from: <https://hdl.handle.net/1887/3425771>

Note: To cite this publication please use the final published version (if applicable).

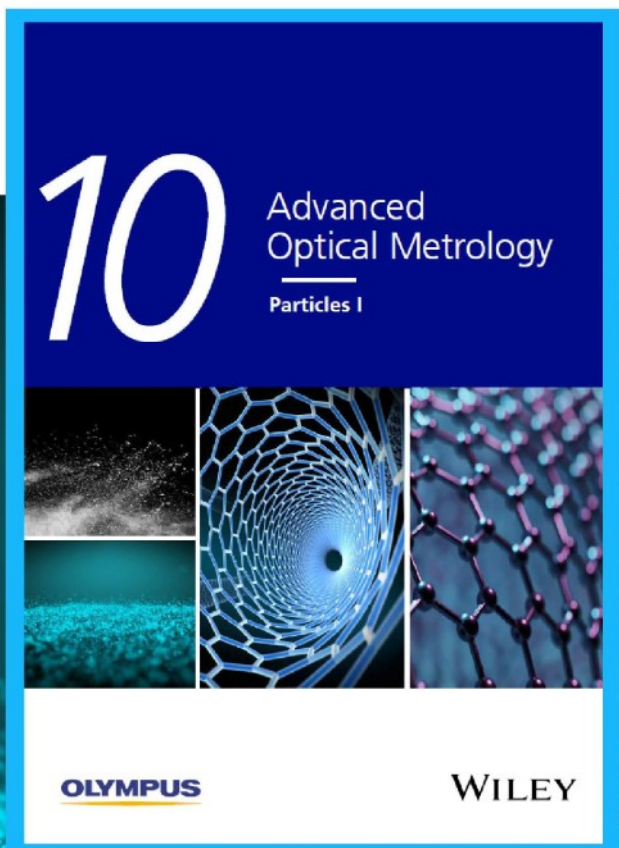


Particles I

Access the latest eBook →

Particles: Unique Properties,
Uncountable Applications

Read the latest eBook and
better your knowledge with
highlights from the recent
studies on the design and
characterization of micro-
and nanoparticles for
different application areas.



[Access Now](#)

This eBook is sponsored by

OLYMPUS

WILEY

Near-Infrared Phototransistor Based on Graphene/ C₆₀/PbPc Heterojunction with Tunable Bidirectional Photoresponse

Qinyong Dai, Gang Hu, Wenli Lv, Sunan Xu, Lei Sun, Grégory F. Schneider, Lin Jiang,*
and Yingquan Peng*

Graphene–organic heterojunction phototransistors have great potential to achieve sensitive photoresponse owing to the excellent absorption of organic layers and fast charge transport in graphene. However, the photoresponse of most graphene-based phototransistors is limited within visible light region with narrow bandwidth and poor sensitivity in the near-infrared (NIR) region. Herein, a graphene–organic NIR phototransistor is fabricated by integrating an organic heterojunction layer composing of phthalocyanine molecules and fullerene C₆₀ onto the graphene channel. The phototransistor exhibits a high photoresponsivity of $2.2 \times 10^3 \text{ A W}^{-1}$ under 850 nm irradiation with the power density of 35.4 mW cm^{-2} ($V_{\text{ds}} = 1 \text{ V}$). Meanwhile, a bidirectional photoresponse (both positive and negative) is obtained at different wavelength regions. Further studies indicate that the gate voltage enables to effectively tune the photoresponse in the wavelength range where PbPc has a significant optical absorption. Such a tunability of photoresponse is especially beneficial for the exploration of new functionalities in logic function devices. This work presents a feasible strategy to prepare graphene–organic heterojunction phototransistor with broadband photoresponse as well as sensitive and tunable bidirectional signals at NIR region.

including the bandwidth, photoresponsivity, and photoconductive gain.^[5,6] To overcome these limitations, graphene hybrid photodetectors incorporating photosensitive materials such as single crystals,^[7] 2D materials,^[8] organic polymers,^[9] colloidal quantum dots,^[10,11] and silicon^[12] have been widely adopted to enhance the photoresponse. For example, methylammonium triiodideplumbate (CH₃NH₃PbI₃) perovskite incorporated with graphene yielded a planar heterojunction photodetector with a broad spectral response from 405 to 800 nm.^[13] Moreover, a hybrid graphene phototransistor adopting organic semiconductor poly (3-hexylthiophene) (P3HT) achieved a high photoresponse up to 10^5 A W^{-1} .^[9] Despite that the combination of photosensitive layers and graphene has proved to be an effective strategy to enhance the performance of phototransistors,^[14–18] the absence of an internal built-in electric field using a single type of light-sensitive layers

leads to relatively low photoresponsivity for photodetection.


Recently, the combination of a PN heterojunction into graphene optoelectronic devices as the absorption layer has been considered as an emerging means to enhance the responsivity and photoconductive gain.^[19,20] The internal built-in electric field within the PN heterojunction enables efficient dissociation for excitons.^[19] Meanwhile, different absorption wavelengths of the PN layers with proper band alignment can lead to unique bidirectional photoresponse, enabling the extension of the photodetection bandwidth.^[21] Recently, a pentacene planar heterojunction was employed to integrate with graphene to fabricate a high-performance transistor, showing bidirectional photoresponse at different wavelength regions with an ultra-wide spectrum detection from 405 to 1550 nm.^[22] Meanwhile, a vertical graphene–C₆₀–graphene heterojunction in a 250×250 photodetector array was assembled to realize a high photoresponsivity of $3.4 \times 10^5 \text{ A W}^{-1}$ ($\lambda = 405 \text{ nm}$, i.e., visible) with bidirectional photocurrent responses.^[23] In spite of the considerable progress made in the last decades to achieve high-performance detection for visible and ultraviolet light, most of the graphene phototransistors are still limited to low photoresponsivity at the near-infrared (NIR) region.

1. Introduction

Graphene has received considerable attention for advanced optoelectronic applications owing to the extraordinary high mobility, wide-range absorption, and tunable doping effect.^[1–4] However, the rapid charge recombination and low light absorption (2.3% of visible and near-infrared light) of graphene largely limit the performance of graphene-based phototransistors

Q. Dai, G. Hu, W. Lv, S. Xu, L. Sun, Y. Peng
Institute of Microelectronics
College of Optical and Electronic Technology
China Jiliang University
Hangzhou 310018, P. R. China
E-mail: yqpeng@cjl.u.edu.cn

G. F. Schneider, L. Jiang
Leiden Institute of Chemistry
Leiden University
Leiden 2333CC, The Netherlands
E-mail: l.jiang.2@lic.leidenuniv.nl

 The ORCID identification number(s) for the author(s) of this article can be found under <https://doi.org/10.1002/admi.202200116>.

DOI: 10.1002/admi.202200116

Herein, we report a NIR graphene photodetector by integrating a PN heterojunction layer of phthalocyanine molecules and fullerene C_{60} with the graphene channel for a broadband photodetection from visible to NIR region. In addition, unique bidirectional photoresponses at different wavelengths and upon gate voltage tuning were achieved. The surface morphology and molecular structures of the proposed graphene phototransistors were characterized. Furthermore, the fabricated graphene/ C_{60} /PbPc phototransistor for the first time achieved the photoresponsivity at the NIR region as high as $2.2 \times 10^3 \text{ A W}^{-1}$. The photoresponsivity and the mechanism of the bidirectional photoresponses of the phototransistor graphene/ C_{60} /PbPc were further investigated. The underlying mechanisms for the gate voltage tuning of bidirectional photoresponse in the wavelength range where PbPc has a significant optical absorption were thoroughly discussed. As a comparison, graphene phototransistors with different combinations of PN layers including PbPc/ C_{60} , C_{60} :PbPc, C_{60} /PbPc, SnPc/ C_{60} have been presented.

2. Results and Discussions

2.1. Fabrication and Characterization of Graphene–Organic Phototransistors

Graphene–organic heterojunction phototransistors were fabricated by depositing bilayers of C_{60} , tin phthalocyanine (SnPc)

or lead phthalocyanine (PbPc) thin films on single-layer graphene grown by chemical vapor deposition (CVD) method (see the Experimental Section). As illustrated in Figure 1a, CVD graphene was transferred onto a heavily doped silicon wafer with thermally grown SiO_2 using polymer assisted method.^[24] After polymer removal using acetone, source and drain electrodes were deposited onto graphene to define the transistor channel ($W \times L = 25 \mu\text{m} \times 2 \text{mm}$). Afterward, thin films of the organic molecules illustrated in Figure 1b were deposited on top of the channel. Our previous work has proved that the incorporation of SnPc and PbPc can significantly improve the photoresponsivity and detectivity of phototransistors in NIR region.^[25,26] Therefore, SnPc and PbPc as the dominant photosensitive layers were integrated with graphene field-effect transistors to further improve the device performance in NIR region. Meanwhile, C_{60} as an ideal electron receptor was selected to construct the PN heterojunction and the build-in electric field to facilitate efficient electron transfer in the heterojunction.^[25,27] The fabricated graphene/ C_{60} /PbPc (Gr/ C_{60} /PbPc) phototransistor in Figure 1a is denoted as device A. Correspondingly, a collection of devices B (Gr/PbPc/ C_{60}) to E (Gr/SnPc/ C_{60}) were also prepared with different heterojunction configurations for comparison and control (Figure S1, Supporting Information).

Raman spectroscopy was employed to characterize the graphene quality and the deposition of organic thin films (Figure 1c). The single layer graphene shows the characteristic G and 2D peaks at 1591 and 2682 cm^{-1} , respectively. The single Lorentz fitted 2D peak reflects the presence of monolayer graphene.^[28]

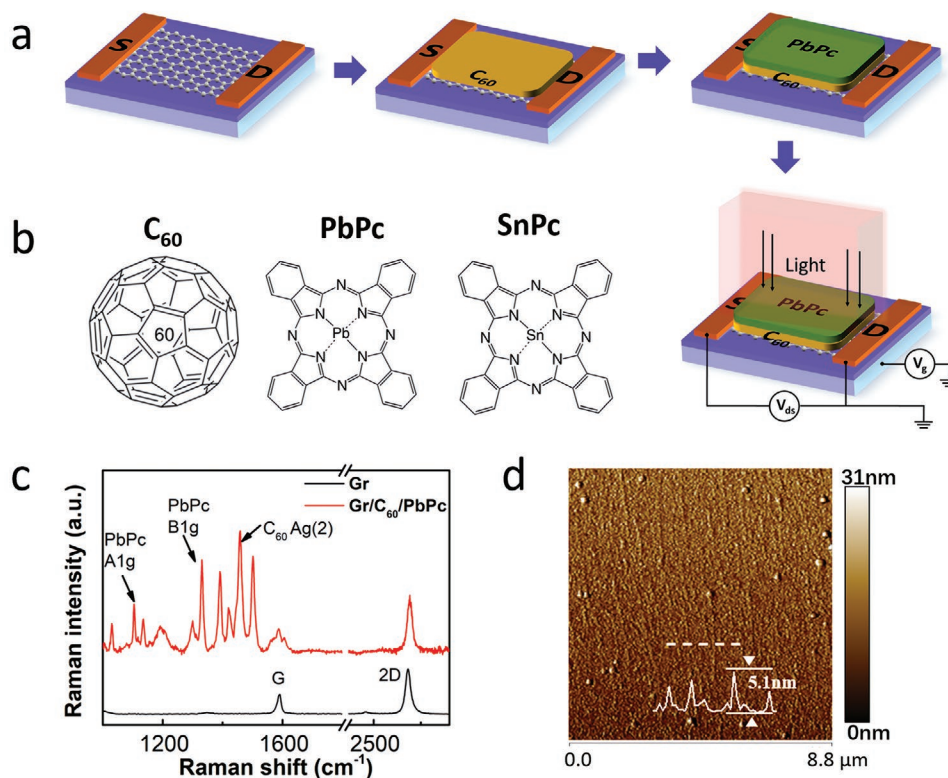


Figure 1. Fabrication and characterization of graphene–organic phototransistors. a) Illustration of device fabrication of Gr/ C_{60} /PbPc phototransistor (device A). b) Molecular structure of C_{60} , PbPc and SnPc. c) Raman spectra of graphene and Gr/ C_{60} /PbPc. d) AFM image of Gr/ C_{60} /PbPc.

The low intensity of D peak at 1350 cm^{-1} indicates the high quality of graphene.^[29] Moreover, the characteristic peaks for C_{60} $A_g(2)$ at 1459 cm^{-1} and PbPc at 1104 cm^{-1} (A_{1g}), 1330 cm^{-1} (B_{1g}) were observed in the heterojunction.^[22,30] The blue shift in 2D peak from 2682 to 2688 cm^{-1} after film deposition suggests the hole doping in graphene upon the contact with organic films. The surface morphology of the device was characterized using atomic force microscopy (AFM), which exhibits a uniform film deposition and a roughness with a magnitude of $\approx 5.1\text{ nm}$.

2.2. Bidirectional Photoresponses of Graphene/ C_{60} /PbPc Phototransistors

Figure 2a depicts the absorption spectra of PbPc (25 nm, black), C_{60} (25 nm, red), the bulk heterojunction film of C_{60} :PbPc (50 nm, blue) with a mixture ratio of 1:1, single layer graphene (pink), planar heterojunction thin films of C_{60} (25 nm)/PbPc (25 nm) (yellow) and graphene/ C_{60} (25 nm)/PbPc (25 nm) (green) on quartz glasses. The PbPc film shows broad and

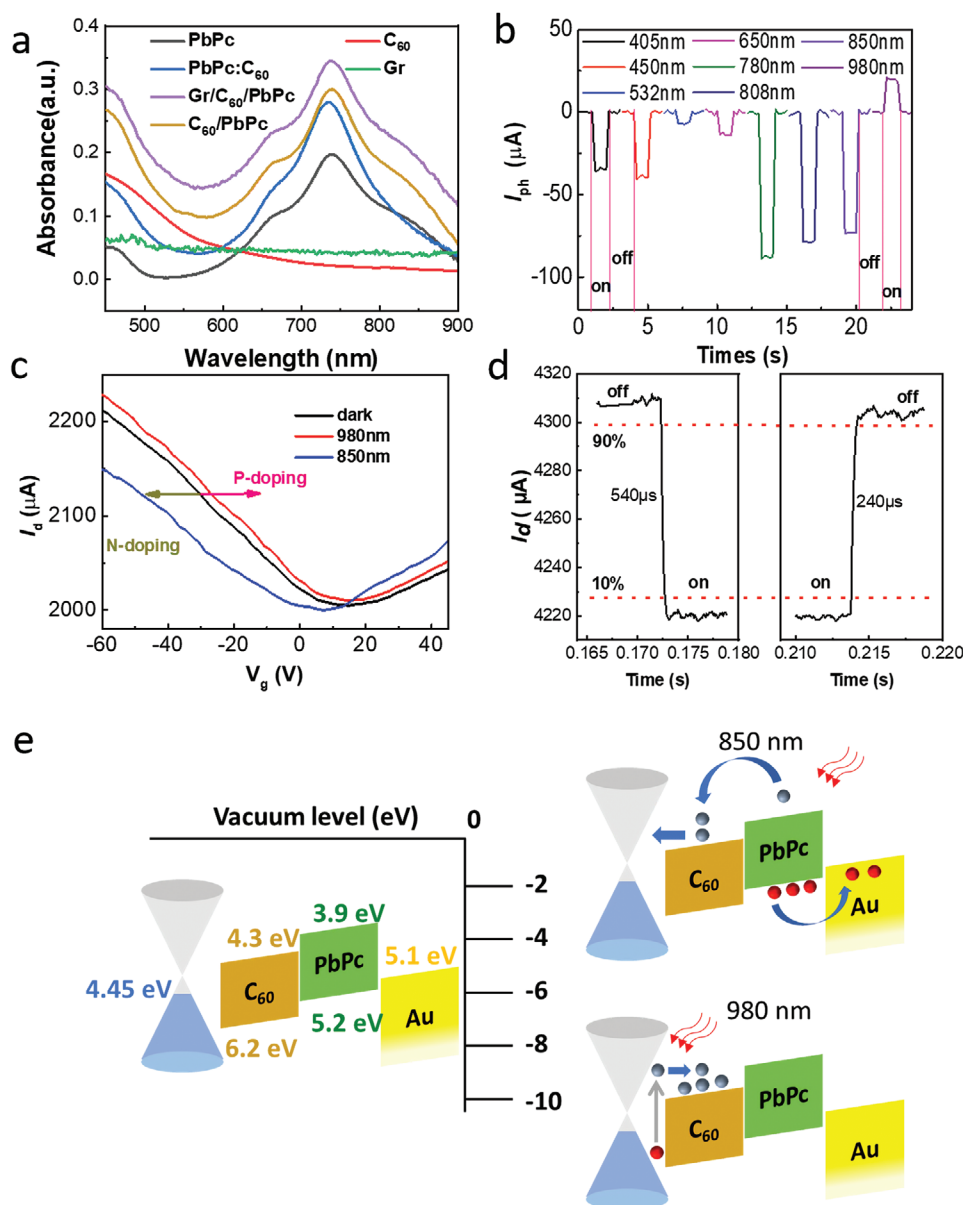


Figure 2. Bidirectional photoresponses based on Gr/ C_{60} /PbPc phototransistors. a) UV-Vis-NIR optical absorption spectra of the thin film of PbPc (25 nm), C_{60} (25 nm), the bulk heterojunction film of C_{60} :PbPc (50 nm) with mixture ratio of 1:1, single layer graphene, planar heterojunction thin films of C_{60} (25 nm)/PbPc (25 nm) and graphene/ C_{60} (25 nm)/PbPc (25 nm). b) The photocurrent at source-drain bias voltages of 1 V and gate voltage of -50 V under different wavelengths radiation with the power density of 40 mW cm^{-2} . c) The transfer characteristics ($V_{ds} = 1\text{ V}$) of device A in dark versus under illumination wavelengths of 850 and 980 nm with the same power density 35.4 mW cm^{-2} . d) The rise and fall times upon irradiation of 850 nm (40 mW cm^{-2}). e) The energy diagram for graphene-organic heterojunction before contact (a Y-axis labeled with specified work function/Fermi level and LUMO/HOMO values) and for the photogenerated carrier transfer process under 850 nm irradiation (negative photoresponse) and under 980 nm irradiation (positive photoresponse).

strong shoulder bands at the NIR region with an absorption peak at 747 nm, which is ascribed to the π - π^* transition from the HOMO to the LUMO of the Pc^{2-} ring.^[31] Meanwhile, the C_{60} film shows almost no absorption at the NIR region. In comparison, graphene covers a wide wavelength range from the ultraviolet to the NIR range with a low absorption, which coincides with the previous reports.^[32,33] The absorption of the C_{60} :PbPc bulk heterojunction film and the planar heterojunction of C_{60} /PbPc shows similar NIR characteristics yet higher intensity compared with PbPc film. The highest NIR absorption is found for the heterojunction graphene/ C_{60} /PbPc with similar peak to PbPc film. Moreover, the thickness of PbPc and C_{60} layers are also designed to maximize the photocurrent. In the heterojunction, thicker PbPc film can generate more photo-generated excitons and thus higher photocurrent. However, excitons generated outside the exciton diffusion length cannot reach the channel for dissociation to generate photo-generated carriers. In addition, great thickness of the photoactive layer will increase the device contact resistance, thus affecting the carrier transport. Above all, the thickness of PbPc film used in this work was 25 nm, which is the upper limit of the exciton diffusion length.^[34–37] Meanwhile, a thin film of C_{60} was used to form the C_{60} /PbPc heterojunction, which is an efficient exciton dissociation interface. To avoid the hole blocking effect induced by thick C_{60} film,^[38–41] a 25 nm C_{60} film was chosen in this work.

The photoresponse of the heterojunction phototransistor was characterized and shown in Figure 2b. The photocurrents of the graphene/ C_{60} /PbPc phototransistor (device A) were measured under the radiations of wavelengths ranging from 405 to 980 nm at a fixed incident power. The source–drain bias voltage was set at 1 V with a gate voltage of -50 V. The signs for the photocurrents were observed to reverse from negative to positive at a wavelength between 850 and 980 nm, which coincides with the cut-off wavelength of the absorption spectra of C_{60} /PbPc shown in Figure 2a. Corresponding to the observed sign reversal, the transport characteristics of the graphene/ C_{60} /PbPc phototransistor show different doping behaviors under different illuminations (Figure 2c). As illustrated in Figure 2c, graphene at dark condition is p-doped with the positive voltage of charge neutrality point (V_{CNP}) of 13 V and the channel conductivity is dominated by hole carriers. The radiation of 850 nm causes n-doping in graphene with the V_{CNP} shifting negatively (from ≈ 13 V at dark to ≈ 7 V). In contrast, the illumination of 980 nm induces p-doping with a positive V_{CNP} shift (from ≈ 13 V at dark to ≈ 17 V). Furthermore, the rise and fall times of photoresponse under irradiation of 850 nm were measured by oscilloscope to characterize the device response time. As shown in Figure 2d, the rise and fall times of the proposed phototransistor are 240 and 540 μs , respectively, which are faster than previous reports.^[10,22] In addition, the degradation test of the photoresponse of the PbPc layer (25 nm) under irradiation were conducted. As shown in Figure S2a,b (Supporting Information), the degradation of light absorption of PbPc upon continuous irradiation of 850 nm within 3 h was negligible. Under the same irradiation, device A also shows excellent photoresponse stability in Figure S2c (Supporting Information).

Taking the above absorption spectra and the transport characteristics into account, the observed bidirectional photoresponse

can be ascribed to a unique band alignment at the NIR-sensitive interfaces within the graphene phototransistors. The energy diagrams for graphene–organic heterojunction before contact and for the photogenerated carrier transfer process under 850 nm irradiation (negative photoresponse) and under 980 nm irradiation (positive photoresponse) are illustrated in Figure 2e. A Y-axis with specified work function/Fermi level and LUMO/HOMO values was labeled on the diagram before contact. In this proposed heterojunction, C_{60} is well-known as the electron acceptor with low LUMO level (4.3 eV) to trap electrons and to facilitate fast charge transfer at C_{60} /donor interface.^[42,43] Therefore, a type-II heterojunction is expected to form upon the contact between C_{60} and PbPc or SnPc.^[44] Based on the absorption characteristics, electron–hole pairs can be generated in both C_{60} and PbPc under the irradiation from 405 to 850 nm. While upon the approaching of NIR region at 850 nm, the PbPc layer acts as the main light-absorbing material. Corresponding to the type-II heterojunction, a built-in electrical field is formed at the interface between PbPc and C_{60} to separate the electron–hole pairs. Electrons are then collected by the graphene channel while holes are trapped within the PbPc layer. Then the collected electrons in the graphene channel result in negative doping (n-doping) in the transport curves (blue line in Figure 2c). As graphene is dominated by hole carriers at the V_g of -50 V, the injected electrons result in the reduction of the hole carrier's density in graphene and thus the observed negative photocurrents in Figure 2b. Namely, the negative photoresponse can be ascribed to the lower photocurrent than the dark current.^[23,45,46] In brief, PbPc and C_{60} serve as the light absorption layer and the carrier separation layer respectively while graphene as the electron conductive channel upon the irradiation of 850 nm (Figure 2e). In contrast, the absorption above 900 nm is expected to mainly originate from graphene (see absorption spectra in Figure 2a). In this scenario, the photogenerated electrons are transferred from graphene to C_{60} (an ideal electron receptor) with graphene acting as a light-absorbing layer and C_{60} as an electron-trapping layer (see the transfer diagram in Figure 2e). As the electrons are collected by C_{60} , the photo-generated holes conducting within graphene contribute to an increase of the hole carrier's density and a p-doping effect (red line in Figure 2c). Correspondingly, the density increase of the hole carriers in p-doped graphene is responsible for the observed positive photoconductivity under 980 nm irradiation.

2.3. Tunable Bidirectional Photoresponses of Graphene/ C_{60} /PbPc Phototransistors

To further investigate the mechanisms of the bidirectional photoresponse of graphene–organic phototransistors under 850 and 980 nm laser irradiations, we performed transient measurements of photoresponse under different gate voltages (Figure 3a,b). The gate voltage enables to modulate the photocurrent by directly tuning the Fermi level of graphene. Figure 3a depicts the photoresponses of graphene/ C_{60} /PbPc phototransistors under 850 nm irradiation. Upon the increase of V_g from -50 to 50 V, the photocurrent changes from negative to positive. In detail, the sign of the photocurrent changes close to $V_g = V_0$, in which V_0 is the V_{CNP} of the transport curve

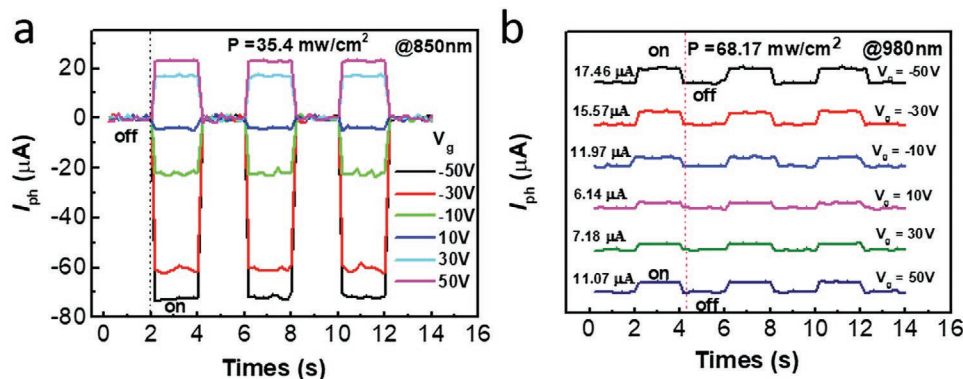


Figure 3. Mechanism analysis of the bidirectional photoresponses. a) Transient measurements at different gate voltages under illumination at 850 nm (power density = 35.4 mW cm⁻², V_{ds} = 1 V). b) Time-dependent photoresponse of 980 nm at different gate voltages (power density = 68.17 mW cm⁻², V_{ds} = 1 V).

under dark condition (as shown in Figure 2c). When $V_g < V_0$, the conductivity in the graphene channel is dominated by hole carriers. The transfer of photogenerated electrons from C₆₀/PbPc to graphene contributes to reducing the hole concentration in graphene, and resulting in a negative photocurrent. Therefore, higher hole concentrations at more negative V_g lead to larger magnitudes of photocurrent. When $V_g > V_0$, electrons are the main carriers in the graphene channel. Correspondingly, the injection of the excited electrons into graphene leads to a density increase of the free electron carriers and thus the positive photocurrent. It is notable that the levels of positive photocurrent for $V_g > V_0$ is relatively lower than negative photocurrent for $V_g < V_0$. Such a contrast can be mainly ascribed to the decreased built-in electric field between graphene and light-absorbing layer upon the change of V_g from negative to positive potentials^[47,48].

Similar measurements were performed under 980 nm laser irradiation (Figure 3b). The inherent positive photocurrent remains to be positive under different gate voltages. The change in the levels of photocurrent upon the increase of V_g from -50 to 50 V is in line with the transport characteristics in Figure 2c. When $V_g < V_0$, the photocurrents decrease from 17.5 to 6.1 μ A upon V_g increasing from -50 to 10 V; whereas $V_g > V_0$, the current values increase from 7.2 to 11.1 μ A with V_g increasing from 10 to 50 V. The built-in electric field is expected to be responsible for the observation in Figure 3b. Under the irradiation of 980 nm incident light, photogenerated holes were transported within graphene while electrons were trapped in C₆₀, forming the built-in electric field (pointed to the graphene from C₆₀ film). When V_g changes from -50 to 10 V, the concentration of dominant hole carriers in graphene decreases, leading to the decreased intensity of the built-in electric field. When V_g increases from 10 to 50 V, the concentration of dominant electron carriers in graphene increases, making the transfer of photogenerated electrons from graphene to C₆₀ easier. As a result, the positive photocurrent keeps increasing with V_g . In addition, thermoelectric effect driven by hot-carrier-assisted transport in graphene is another possible explanation for the observed change of positive photocurrent.^[49] In the phototransistor, the photovoltage produced by the photogenerated hot electrons can be related to the electrical conductivity of

graphene based on the Mott formula.^[50] Thus, the thermoelectric photovoltage follows the dependency of the conductance on the carrier density, which agrees well with the observed photocurrent in Figure 3b. Specifically, the increases of V_g shift the levels of carrier density in graphene from high to low ($V_g < V_0$) and then from low to high ($V_g > V_0$), leading to the corresponding changes in the photo-thermoelectric conductivity.

2.4. Photoresponse and Responsivity of Graphene/C₆₀/PbPc Phototransistors

Next, we measured the time-dependent photoresponses and photoresponsivity of device A upon the irradiation of 850 nm. Figure 4a shows the time-dependent photoresponse of device A under various light intensities at V_{ds} = 1 V and V_g = -50 V under 850 nm lasers illumination. In addition to the stable NIR detection, the photocurrent increases gradually with the light intensity, which can be attributed to the photoconductivity effect and the photoelectric effect in the phototransistor.^[51]

Figure 4b shows the dependence of photocurrent (I_{ph}) and photoresponsivity (R) on the incident light power under 850 nm laser illumination. The photoresponsivity (R) was measured and calculated based on the following equation^[52]

$$R = \frac{|I_{ill}| - |I_{dark}|}{P_{opt}} = \frac{I_{ph}}{A \cdot P_{int}} \quad (1)$$

where P_{opt} is the incident optical power on the device, P_{int} is the incident optical intensity, and A is the effective irradiated area of the device. As shown in Figure 4b, the responsivity decreases upon the increase of incident power, which is hypothesized to be ascribed to the gradually filled trap states within the heterojunction. Once the trap states in the device are filled completely at a certain irradiation intensity, more incident light only induced carriers recombine instead. Then it is less likely for the device to capture more carriers excited by a stronger light power, thus leading to a reduction in the average carrier lifetime and reduced responsivity.^[11,53–56] Under NIR (λ = 850 nm) illumination, the calculated maximum photoresponsivity is up to 2.2×10^3 (± 178) A W⁻¹ while keeping source–drain bias

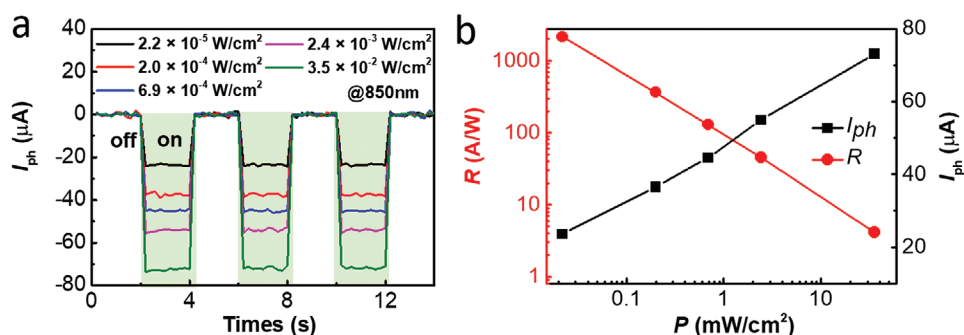


Figure 4. Characteristics of time-dependent photoresponse and responsivity of graphene/ C_{60} /PbPc phototransistors. a) Time-dependent photoresponse of device A under various light intensities at $V_{ds} = 1$ V and $V_g = -50$ V under 850 nm lasers illumination. The “on” regions are labeled with green shadow rectangles. b) Dependence of photocurrent (I_{ph}) and photoresponsivity (R) on incident light power under 850 nm laser illumination for the device A.

voltages V_{sd} at 1 V, V_g (gate voltage) of -50 V and the power density of $22 \mu\text{W cm}^{-2}$. The performance of sensitized graphene phototransistors with similar heterojunction structures or light-collecting materials are summarized in **Table 1**. It is noteworthy that the reported high responsivity of most graphene-based devices is mainly limited in the ultraviolet and visible region. The photoresponses at NIR region in previous reports are generally low as the NIR light is only absorbed by graphene. In contrast, PbPc in our graphene/ C_{60} /PbPc heterojunction has an excellent NIR absorption, thus leading to the high photoresponsivity at the NIR region. Such excellent photoresponses are also highly related to the fast charge transfer at the graphene/ C_{60} interface and high dissociation efficiency of the excitons at the C_{60} /PbPc interface.

Table 1. Comparison of the photoresponses of graphene-based phototransistors.

Active materials	Responsivity [A W^{-1}]	Spectral range [nm]	Ref.
Graphene/PTCDA/pentacene	1×10^5	400–700	[19]
Graphene/perovskite ($\text{CH}_3\text{NH}_3\text{PbI}_3$)	1.8×10^2	400–800	[13]
Graphene/SWNTs	1.0×10^2	400–1550	[57]
Graphene/ C_8 -BTBT	1.0×10^4	355	[58]
SWNTs/ C_{60}	2.0×10^2	1000–1400	[59]
Graphene/P3HT	1.0×10^5	500	[9]
Graphene/P3HT/perovskite ($\text{CH}_3\text{NH}_3\text{PbI}_{3-x}\text{Cl}_x$)	4.3×10^9	400–800	[20]
Graphene/chlorophyll	1.0×10^6	400–700	[60]
Graphene/rubrene	1.0×10^7	400–600	[7]
Graphene/ WS_2	1.0×10^6	400–700	[8]
Graphene/PbS QDS	1.0×10^7	600–1000	[61]
$\text{MoS}_2/\text{g-C}_3\text{N}_4$	4.0×10^0	270	[62]
Graphene/ C_{60}	1.1×10^2	405–1550	[63]
Graphene/ C_{60} /pentacene	9.1×10^2	405–1550	[22]
Graphene/ C_{60} /graphene (vertical)	3.4×10^5	405–1550	[64]
Graphene/ C_{60} /graphene (planar)	5.5×10^3	360–658	[65]
Graphene/ C_{60} /PbPc	2.2×10^3	405–980	This work

2.5. The Optimization of Phototransistor Fabrication

To further investigate the mechanism of the observed bidirectional photoresponse, we fabricated another two hybrid phototransistors exhibiting similar structures with graphene/ C_{60} /PbPc (device A). As shown in Figure S1 (Supporting Information), Gr/PbPc (25 nm)/ C_{60} (25 nm) and Gr/ C_{60} :PbPc (50 nm) with mixture ratio of 1:1 were prepared and referred to as device B (Gr/PbPc/ C_{60}) and device C (Gr/ C_{60} :PbPc), respectively. For the PbPc: C_{60} bulk heterojunction, the increase of the PbPc ratio help to improve the NIR light absorption, while the decrease of the C_{60} ratio leads to the reduction of the exciton dissociation interface and thus affects the photocurrent. Therefore, the ratio of PbPc: C_{60} was optimized to be 7:3 in Figure S4e (Supporting Information). In these two devices, graphene is not in direct contact with a thin film of C_{60} , which is the main difference with device A. As a result, device B showed a limited photoresponsivity in NIR region with a value of 418 A W^{-1} (Figure S3, Supporting Information), whereas device C shows an even lower value of 218 A W^{-1} (Figure S4, Supporting Information). Such inferior photoresponse of device B and C compared to device A suggest that C_{60} thin film in direct contact with graphene is critical to enhance the responsivity. Especially, device C (Gr/PbPc: C_{60}) as the bulk heterojunction device is featured for an interpenetrating network of donor and acceptor materials with maximized and discrete interfaces.^[66,67] Such a network makes it feasible to dissociate the excitons to separated holes and electrons. Yet the charge transfer from acceptor to graphene in device C is inferior to the planar heterojunction of Gr/ C_{60} /PbPc as device A.^[68,69] In device A, a direct contact between graphene and C_{60} as the acceptor guarantees a more efficient charge transfer and thus higher photoresponsivity. Due to the similar sp^2 hybridized carbon lattice between graphene and C_{60} , an excellent epitaxial condition for C_{60} molecules can be formed via van der Waals (vdW) interaction and intermolecular π - π stacking interaction to result in a compact and firmly bonded graphene/ C_{60} interface.^[13,64,70] Moreover, it is also reported that C_{60} film on graphene is more uniform than on Si/SiO₂ substrate.^[63] The results in this work confirm that a uniform and compact C_{60} film proves to be critical for an efficient electron transfer at the interface and thus the fabrication of high-performance graphene phototransistor. Notably, a clean

and uniform surface of graphene is also important to form a compact and high quality heterojunction.^[71,72]

Moreover, graphene/C₆₀/PbPc/Au phototransistor was fabricated and referred to as device D to evaluate the impact of the position of the C₆₀ acceptor layer within the three-layer planar heterojunction (Figure S5c, Supporting Information).^[1,2] The difference between device A and device D is the position of source and drain electrodes (Au) within the heterojunction. In device A, the electrodes are in direct contact with graphene channel; while in device D, the electrodes are deposited directly on top of the organic films. Under the irradiation of 850 nm, device D shows a much lower photoresponsivity (813 A W⁻¹, Figure S5a,d, Supporting Information) than that of device A (2.2 × 10³ A W⁻¹). The explanation for the superior photoresponsivity for device A is related to the elimination of carrier injection barrier at the interface of source electrode and organic layer by depositing organic films directly on top of source and drain electrodes. Therefore, the direct deposition method used for device A proves to be an important strategy to improve carrier injection. In addition, device E with SnPc as the light-absorption layer was fabricated to better understand the role of phthalocyanine materials in determining the device performance (Figure S6a, Supporting Information). The measurement was examined under the same condition with device D. It is shown that device E exhibits similar performance (285 A W⁻¹, Figure S6, Supporting Information) with device D, indicating that SnPc and PbPc are both suitable for combining with graphene to improve the photodetection performance of the graphene-based phototransistor at the NIR region.

3. Conclusions

In this work, we have proposed a graphene/C₆₀/PbPc heterojunction phototransistor with a high photoresponsivity of 2.2 × 10³ A W⁻¹ under 850 nm irradiation and a broadband response between 405 and 980 nm. The remarkable NIR absorption of PbPc, the high dissociation efficiency for the excitons at the PbPc/C₆₀ interface, and the efficient charge transfer at the graphene/C₆₀ interface contribute to such a prominent photoresponsivity at NIR region. In particular, the compact interface of graphene-C₆₀ forming a proper band alignment was the key to achieve high photoresponsivity and bidirectional response at the wavelengths from 405 to 980 nm. Such a bidirectional transport of photoexcitons within the heterojunction proves to be a new strategy to facilitate a broadband photodetection. Moreover, the gate-voltage enables to effectively tune the direction and magnitude of photoresponse within the absorption region of PbPc (405–850 nm). Namely, the photocurrent is negative for V_g > V_{CNP}, and positive for V_g < V_{CNP}. This work not only provides new insights into fabricating phototransistors with broadband detection, but also sheds light into the fundamental understanding and rational design of bidirectional photoresponse of heterojunction-based phototransistors. The tunable photoresponses and scalability of the proposed graphene–organic phototransistors can promote large-scale and high-throughput graphene based NIR phototransistor for high performance photodetection and imaging applications.

4. Experimental Section

Chemical and Materials: PbPc, C₆₀, SnPc (all materials ≥99.5%), ammonium persulfate ((NH₄)₂S₂O₈, ≥98.0%), and n⁺ Si/SiO₂ wafers (SiO₂ 1000 nm) were purchased from commercial suppliers and used as received unless noted otherwise. Chemical vapor deposition (CVD) graphene was grown on a polycrystalline copper foil (Alfa Aesar, 99.999% purity, 25 μm thickness) using a hot-wall chamber supplied by planarGROW-2B, planarTECH. In an atmosphere of H₂ (g, 40 mTorr), the copper foil was annealed and stabilized at 1035 °C. Then the graphene was grown at the surface of the annealed copper by introducing 35 sccm CH₄ (g, 500 mTorr) for a desired period.

Graphene Field-Effect Transistor Fabrication: Prior to transfer the graphene and deposition of active layer, the silicon wafer was ultrasonically cleaned in acetone, ethanol, and deionized water, and then were dried by blowing high-pure N₂. Polymethyl methacrylate (PMMA) was employed to assist the transfer of graphene onto a silicon wafer (topping with a 1000 nm thick oxide layer). PMMA was spin-coated onto the as-grown CVD graphene to form a carrier film after curing. Then the underlying copper was etched in ammonium persulfate solution and rinsed in deionized water to leave the PMMA–graphene layer floating on water. PMMA–graphene was transferred onto silicon wafer cleaned by acetone, isopropanol and deionized water, respectively. Graphene was exposed by removing PMMA using acetone and isopropanol.

For the active layer fabrication of each device, different organic films were vacuum deposited using thermal evaporation technology under vacuum conditions (3.0 × 10⁻⁴ Pa). The crucible temperature was then ramped up for C₆₀ (0.2 Å s⁻¹) and PbPc (0.2–0.3 Å s⁻¹) growth at preoptimized growth conditions, e.g., at a growth temperature in the range of 420–470 °C. And then Au source/drain electrodes were deposited through a lithography mask to define a channel length (L)/width (W) of 25 μm/2 mm.

Device Characterization: Raman spectroscopy was measured using HORIBA LabRAM HR-800, with 532-nm excitation laser under ambient conditions. To minimize the laser induced damage, the Raman laser was controlled at a wavelength of 532 nm with the power of 2 mW. AFM was conducted by Bruker Dimension Icon using the tapping mode at a scan rate of 1 Hz.

Optical and Electrical Measurement: For optical absorption measurements, thin films of single layer graphene, C₆₀ (25 nm) and PbPc (25 nm), planar heterojunction thin films of graphene/C₆₀ (25 nm)/PbPc (25 nm), and the bulk heterojunction film of C₆₀/PbPc (50 nm) with mixture ratio of 1:1 were deposited on cleaned quartz substrates, respectively. The thickness was controlled following the process calibration of the thermal evaporator. Absorption spectra were measured by TU-1901 spectrometer (TLS3-X150-ZGJLDZ). After device fabrication, the samples were immediately transferred into a vacuum chamber (vacuum level ≈10 Pa) and were measured by using an organic semiconductor characterization system (OSDmeas8.0). For the measurements of photo effects, NIR laser diodes with a light intensity of 200 mW cm⁻² for different wavelengths including 405 nm (HW405AD5-10BD), 532 nm (HW532AD5-22BD), 650 nm (HW650AD5-10BD), 780 nm (HW780AD5-10BD), 808 nm (HW808AD5-10BD), 850 nm (HW850AD5-10BD), 905 nm (HW905AD5-10TBC), 980 nm (HW980AD5-10BD) were used. The power and diameter were 5 mW and 10 × 30 mm, respectively. The variation of incident optical power density was realized by inserting neutral filters before the laser diode. Light response time measurements were carried out with a semiconductor parameter analyzer (Agilent B1500) with a vacuum condition of 10⁻³ Torr. A 850 nm NIR-light-emitting diode (LED) (850 nm LEDs for multispectral sensing) driven by a signal generator was used as a light source to illuminate devices from the top.

Supporting Information

Supporting Information is available from the Wiley Online Library or from the author.

Acknowledgements

Q.D. and G.H. contributed equally to this work. This work was financially supported by the Natural Science Foundation of Zhejiang Province Grant No. LQ19F040003, and National Key R&D Program of China Grant No. 2016YFF0203605. L.J. and G.F.S. acknowledge funding from the Chinese Scholarship Council (201406890016), NWA route “meten & detecteren (NWA. 1306.19.005),” the European Research Council under the European Union’s Seventh Framework Program (FP/2007–2013)/ERC Grant Agreement No. 335879 project acronym “Biographene,” and the Netherlands Organization for Scientific Research (Vidi 723.013.007).

Conflict of Interest

The authors declare no conflict of interest.

Data Availability Statement

The data that support the findings of this study are available from the corresponding author upon reasonable request.

Keywords

Graphene–organic phototransistor, phthalocyanine, near-infrared detection, bidirectional photoresponse

Received: January 18, 2022

Revised: May 5, 2022

Published online:

- [1] Z. Liu, Q. Liu, Y. Huang, Y. Ma, S. Yin, X. Zhang, W. Sun, Y. Chen, *Adv. Mater.* **2008**, *20*, 3924.
- [2] P. B. R. R. Nair, A. N. Grigorenko, K. S. Novoselov, T. J. Booth, T. Stauber, N. M. R. Peres, A. K. Geim, *Science* **2008**, *320*, 1308.
- [3] C. X. Guo, H. B. Yang, Z. M. Sheng, Z. S. Lu, Q. L. Song, C. M. Li, *Angew. Chem., Int. Ed. Engl.* **2010**, *49*, 3014.
- [4] Z. Yin, J. Zhu, Q. He, X. Cao, C. Tan, H. Chen, Q. Yan, H. Zhang, *Adv. Energy Mater.* **2014**, *4*, 1300574.
- [5] F. Xia, H. Wang, D. Xiao, M. Dubey, A. Ramasubramaniam, *Nat. Photonics* **2014**, *8*, 899.
- [6] F. Bonaccorso, Z. Sun, T. Hasan, A. C. Ferrari, *Nat. Photonics* **2010**, *4*, 611.
- [7] G. F. Jones, R. M. Pinto, A. De Sanctis, V. K. Nagareddy, C. D. Wright, H. Alves, M. F. Craciun, S. Russo, *Adv. Mater.* **2017**, *29*, 1702993.
- [8] J. D. Mehew, S. Unal, E. Torres Alonso, G. F. Jones, S. Fadhil Ramadhani, M. F. Craciun, S. Russo, *Adv. Mater.* **2017**, *29*, 1700222.
- [9] E. H. Huisman, A. G. Shulga, P. J. Zomer, N. Tombros, D. Bartsch, S. Z. Bisri, M. A. Loi, L. J. Koster, B. J. van Wees, *ACS Appl. Mater. Interfaces* **2015**, *7*, 11083.
- [10] R. Pan, H. Li, J. Wang, X. Jin, Q. Li, Z. Wu, J. Gou, Y. Jiang, Y. Song, *Part. Part. Syst. Character.* **2018**, *35*, 1700304.
- [11] G. Konstantatos, M. Badioli, L. Gaudreau, J. Osmond, M. Bernechea, F. P. Garcia de Arquer, F. Gatti, F. H. Koppens, *Nat. Nanotechnol.* **2012**, *7*, 363.
- [12] J. Liu, Y. Yin, L. Yu, Y. Shi, D. Liang, D. Dai, *Sci. Rep.* **2017**, *7*, 40904.
- [13] Y. Lee, J. Kwon, E. Hwang, C. H. Ra, W. J. Yoo, J. H. Ahn, J. H. Park, J. H. Cho, *Adv. Mater.* **2015**, *27*, 41.
- [14] L. B. Luo, L. H. Zeng, C. Xie, Y. Q. Yu, F. X. Liang, C. Y. Wu, L. Wang, J. G. Hu, *Sci. Rep.* **2014**, *4*, 3914.
- [15] M. K. Thakur, C. Y. Fang, Y. T. Yang, T. A. Effendi, P. K. Roy, R. S. Chen, K. K. Ostrikov, W. H. Chiang, S. Chattopadhyay, *ACS Appl. Mater. Interfaces* **2020**, *12*, 28550.
- [16] S. Ghosh, W. C. Chiang, M. Y. Fakhri, C. T. Wu, R. S. Chen, S. Chattopadhyay, *Nano Energy* **2020**, *67*, 104258.
- [17] M. K. Thakur, A. Gupta, M. Y. Fakhri, R. S. Chen, C. T. Wu, K. H. Lin, S. Chattopadhyay, *Nanoscale* **2019**, *11*, 9716.
- [18] M. Kataria, K. Yadav, G. Haider, Y. M. Liao, Y.-R. Liou, S.-Y. Cai, H.-i. Lin, Y. H. Chen, C. R. Paul Inbaraj, K. P. Bera, H. M. Lee, Y.-T. Chen, W.-H. Wang, Y. F. Chen, *ACS Photonics* **2018**, *5*, 2336.
- [19] X. Chen, X. Liu, B. Wu, H. Nan, H. Guo, Z. Ni, F. Wang, X. Wang, Y. Shi, X. Wang, *Nano Lett.* **2017**, *17*, 6391.
- [20] C. Xie, F. Yan, *ACS Appl. Mater. Interfaces* **2017**, *9*, 1569.
- [21] U. Hrozhyk, v. SSerak, N. Tabiryan, T. J. White, T. J. Bunning, *Opt. Express* **2009**, *17*, 716.
- [22] J. Han, J. Wang, M. Yang, X. Kong, X. Chen, Z. Huang, H. Guo, J. Gou, S. Tao, Z. Liu, Z. Wu, Y. Jiang, X. Wang, *Adv. Mater.* **2018**, *30*, 1804020.
- [23] R. Pan, J. Han, X. Zhang, Q. Han, H. Zhou, X. Liu, J. Gou, Y. Jiang, J. Wang, *Carbon* **2020**, *162*, 375.
- [24] X. Liang, B. A. Sperling, I. Calizo, G. Cheng, C. A. Hacker, Q. Zhang, Y. Obeng, K. Yan, H. Peng, Q. Li, X. Zhu, H. Yuan, A. R. H. Walker, Z. Liu, L.-m. Peng, C. A. Richter, *ACS Nano* **2011**, *5*, 9144.
- [25] F. Huang, Y. Li, H. Xia, J. Zhang, K. Xu, Y. Peng, G. Liu, *Carbon* **2017**, *118*, 666.
- [26] Y. Liang, W. Lv, X. Luo, L. He, K. Xu, F. Zhao, F. Huang, F. Lu, Y. Peng, *Synth. Met.* **2018**, *240*, 44.
- [27] S. Park, S. J. Kim, J. H. Nam, G. Pitner, T. H. Lee, A. L. Ayzner, H. Wang, S. W. Fong, M. Vosgueritchian, Y. J. Park, M. L. Brongersma, Z. Bao, *Adv. Mater.* **2015**, *27*, 759.
- [28] C. B. Flores, R. Y. Sato-Berru, D. Mendoza, *Appl. Phys. Lett.* **2014**, *105*, 191116.
- [29] A. Eckmann, A. Felten, A. Mishchenko, L. Britnell, R. Krupke, K. S. Novoselov, C. Casiraghi, *Nano Lett.* **2012**, *12*, 3925.
- [30] X. Ling, W. Fang, Y. H. Lee, P. T. Araujo, X. Zhang, J. F. Rodriguez-Nieva, Y. Lin, J. Zhang, J. Kong, M. S. Dresselhaus, *Nano Lett.* **2014**, *14*, 3033.
- [31] A. A. Fadda, R. E. El-Mekawy, N. N. Soliman, A. M. Allam, M. T. J. D. Abdelaal, *Dyes Pigm.* **2018**, *155*, 300.
- [32] R. R. Nair, P. Blake, A. N. Grigorenko, K. S. Novoselov, T. J. Booth, T. P. Stauber, N. M. R. , A. K. Geim, *Science* **2008**, *320*, 1308.
- [33] R. D. Tamas, M. Vladescu, I. Cristea, B. Tincu, I. Demetrescu, M. Popescu, I. Mihalache, F. Comanescu, T. Burinaru, C. Marculescu, A. Matei, V. Tucureanu, A. Marioara, A. Avram, *Proc. SPIE* **2018**, *10977*, 109770C.
- [34] Q. Dai, K. Xu, Y. Peng, W. Lv, Z. Zhao, L. Sun, Y. Wang, Q. Li, H. Zhu, Z. Zhou, C. Gu, *Infrared Phys. Technol.* **2020**, *108*, 103358.
- [35] W. A. Luhman, R. J. Holmes, *Adv. Funct. Mater.* **2011**, *21*, 764.
- [36] T. K. Mullenbach, I. J. Curtin, T. Zhang, R. J. Holmes, *Nat. Commun.* **2017**, *8*, 14215.
- [37] T. M. Kim, H. S. Shim, M. S. Choi, H. J. Kim, J. J. Kim, *Appl. Mater. Interfaces* **2014**, *6*, 4286.
- [38] Z. Zhou, G. Liao, X. Song, Q. Dai, L. Sun, Y. Peng, P. Wang, *Nanoscale Res. Lett.* **2022**, *17*, 19.
- [39] Y. Wang, R. Ding, F. Huang, D. Ma, *Synth. Met.* **2018**, *244*, 61.
- [40] B. Yao, Y. Li, Z. Wen, M. Zhou, Wenli, L. J. S. Metals, *Synth. Met.* **2014**, *193*, 35.
- [41] D. Chen, B. Yao, G. Fan, W. Lv, P. Gao, M. Zhou, Y. Peng, *Appl. Phys. Lett.* **2013**, *102*, 162106.
- [42] D. Yu, K. Park, M. Durstock, L. Dai, *J. Phys. Chem. Lett.* **2011**, *2*, 1113.
- [43] G. J. Dutton, W. Jin, J. E. Reutt-Robey, S. W. Robey, *Phys. Rev. B* **2010**, *82*, 073407.
- [44] S. Lee, J. C. Flanagan, J. Kang, J. Kim, M. Shim, B. Park, *Sci. Rep.* **2015**, *5*, 17472.
- [45] V. T. Nguyen, Y. C. Kim, Y. H. Ahn, S. Lee, J.-Y. Park, *Carbon* **2020**, *168*, 580.

- [46] Y. Chen, X. Wang, G. Wu, Z. Wang, H. Fang, T. Lin, S. Sun, H. Shen, W. Hu, J. Wang, J. Sun, X. Meng, J. Chu, *Small* **2018**, *14*, 1703293.
- [47] X. Xu, N. M. Gabor, J. S. Alden, A. M. van der Zande, P. L. McEuen, *Nano Lett.* **2010**, *10*, 562.
- [48] K. Roy, M. Padmanabhan, S. Goswami, T. P. Sai, G. Ramalingam, S. Raghavan, A. Ghosh, *Nat. Nanotechnol.* **2013**, *8*, 826.
- [49] F. H. Koppens, T. Mueller, P. Avouris, A. C. Ferrari, M. S. Vitiello, M. Polini, *Nat. Nanotechnol.* **2014**, *9*, 780.
- [50] N. W. Ashcroft, N. D. Mermin, *Solid State Physics*, Saunders College, Philadelphia **1976**, p. 120.
- [51] R. J. Nelson, *Appl. Phys. Lett.* **1977**, *31*, 351.
- [52] K. J. Baeg, M. Binda, D. Natali, M. Caironi, Y. Y. Noh, *Adv. Mater.* **2013**, *25*, 4267.
- [53] L. Jiang, W. Fu, Y. Y. Birdja, M. T. M. Koper, G. F. Schneider, *Nat. Commun.* **2018**, *9*, 793.
- [54] H. Fang, W. Hu, *Adv. Sci. (Weinh)* **2017**, *4*, 1700323.
- [55] D. H. Shin, S. H. Choi, *Micromachines* **2018**, *9*, 350.
- [56] J. Jiang, C. Ling, T. Xu, W. Wang, X. Niu, A. Zafar, Z. Yan, X. Wang, Y. You, L. Sun, J. Lu, J. Wang, Z. Ni, *Adv. Mater.* **2018**, 1804332.
- [57] K. K. K. Hong-Zhang Geng, Kang Pyo So, Young Sil Lee, Youngkyu Chang, Young Hee Lee, *JACS Commun.* **2007**, 129, 7758.
- [58] X. Liu, X. Luo, H. Nan, H. Guo, P. Wang, L. Zhang, M. Zhou, Z. Yang, Y. Shi, W. Hu, Z. Ni, T. Qiu, Z. Yu, J. B. Xu, X. Wang, *Adv. Mater.* **2016**, *28*, 5200.
- [59] H. Zhou, M. Yang, C. Ji, X. Liu, R. Pan, Q. Han, J. Wang, Y. Jiang, *ACS Sustainable Chem. Eng.* **2020**, *8*, 4276.
- [60] S.-Y. Chen, Y.-Y. Lu, F.-Y. Shih, P.-H. Ho, Y.-F. Chen, C.-W. Chen, Y.-T. Chen, W.-H. Wang, *Carbon* **2013**, *63*, 23.
- [61] Y. Che, X. Cao, Y. Zhang, J. Yao, *Photonics Nanostruct. – Fundam. Appl.* **2021**, *43*, 100866.
- [62] D. B. Velusamy, M. A. Haque, M. R. Parida, F. Zhang, T. Wu, O. F. Mohammed, H. N. Alshareef, *Adv. Funct. Mater.* **2017**, *27*, 1605554.
- [63] S. Qin, X. Chen, Q. Du, Z. Nie, X. Wang, H. Lu, X. Wang, K. Liu, Y. Xu, Y. Shi, R. Zhang, F. Wang, *ACS Appl. Mater. Interfaces* **2018**, *10*, 38326.
- [64] K. Kim, T. H. Lee, E. J. Santos, P. S. Jo, A. Salleo, Y. Nishi, Z. Bao, *ACS Nano* **2015**, *9*, 5922.
- [65] S. Qin, H. Jiang, Q. Du, Z. Nie, X. Wang, W. Wang, X. Wang, Y. Xu, Y. Shi, R. Zhang, F. Wang, *Carbon* **2019**, *146*, 486.
- [66] F. Yang, M. Shtein, S. R. Forrest, *Nat. Mater.* **2004**, *4*, 37.
- [67] W. Chen, T. Xu, F. He, W. Wang, C. Wang, J. Strzalka, Y. Liu, J. Wen, D. J. Miller, J. Chen, K. Hong, L. Yu, S. B. Darling, *Nano Lett.* **2011**, *11*, 3707.
- [68] C. Uhrich, D. Wynands, S. Olthof, M. K. Riede, K. Leo, S. Sonntag, B. Maennig, M. Pfeiffer, *J. Appl. Phys.* **2008**, *104*, 043107.
- [69] K. Nakano, K. Tajima, *Adv. Mater.* **2017**, *29*, 1603269.
- [70] Y.-H. Chen, M. Kataria, H.-I. Lin, C. R. Paul Inbaraj, Y.-M. Liao, H.-W. Hu, T.-J. Chang, C.-H. Lu, W.-H. Shih, W.-H. Wang, Y.-F. Chen, *ACS Appl. Electron. Mater.* **2019**, *1*, 1517.
- [71] L. Jiang, P. M. van Deursen, H. Arjmandi-Tash, L. A. Belyaeva, H. Qi, J. He, V. Kofman, L. Wu, V. Muravev, U. Kaiser, *Sci. China: Chem.* **2021**, *64*, 1047.
- [72] L. Jiang, W. Fu, Y. Y. Birdja, M. T. Koper, G. F. Schneider, *Nat. Commun.* **2018**, *9*, 793.